Journal of Naval Architecture and Marine Engineering
July, 2026
https://doi.org/10.3329/jname.v23i2.84889 https://www.banglajol.info

MFD CASSON-WILLIAMSON FLUID FLOW ACROSS AN INCLINED STRETCHING SURFACE WITH RADIATIVE HEAT

Yathiraj S.[1*], Murulidhara N.[2], Jeevankumar[3], and Ali J. Chamkha[4]

[1]Department of Mathematics. Sri Siddhartha Academy of Higher Education, Tumakuru-572 107, India.
[2]Department of Mathematics, Sri Siddhartha Institute of Technology, Tumakuru-572 105, India.
[3]Department of Mathematics, Karnatak Arts, Science and Commerce College, Bidar-585 401, India.
[4]Faculty of Engineering, Kuwait College of Science and Technology, Doha District-35004, Kuwait.
Email: [1*]yathiraj4952@gmail.com, [2]muru26676@gmail.com, [3]jeevankumarpavar@gmail.com, [4]achamkha@yahoo.com

Abstract:

This study investigates the magneto fluid dynamic (MFD) Casson-Williamson fluid (CWF) flow of reaction with chemicals and the effect of thermal radiation on an inclined plane at an angle γ on a stretching surface. Our main goal is to understand the impact of the magnetic field and the Lewis number on the transfer of heat. The framework involves converting partial differential equations (PDEs) into ordinary differential equations (ODEs) using suitable techniques. ODEs are solved using MATLAB through the BVP4C method, which employs a finite difference approach. The comparable inferences that were considered for the Williamson and Casson fluid are presented in graphs and tables. Moreover, the research examines the effects of key dimensionless parameters on the flow, heat and mass transfer characteristics of the system. An increase in the magnetic parameter reduces fluid velocity due to the Lorentz force while enhancing energy generation within the flow. Higher Prandtl number decrease temperature field and intensify fluid motion buoyancy effects. The analysis covers heat generation in MFD CWF, with a detailed assessment of the transfer of heat on a stretching surface in an inclined plane at an angle γ with a permeable surface.

Keywords: Thermal radiation, heat transfer, stretching surface, magneto fluid dynamics, Casson-Williamson fluid

NOMENCLATURE

b : Stretching rate(s^{-1})
C_f : Skin friction coefficient(-)
C_p : Heat capacity at constant pressure($JKg^{-1}K^{-1}$)
D_B : Coefficient of Brownian Diffusion(m^2s^{-1})
D_T : Coefficient of Thermophoretic Diffusion(m^2s^{-1})
Ec : Eckert number(-)
f : Dimensionless fluid motion variable(-)
f_w : Suction parameter(-)
Fr : Forchheimer number(-)
g : Gravitational force(ms^{-2})
G : Chemical reaction coefficient(-)
Gc : Solutal factor(-)
Gr : Grashof number(-)
k : Thermal conductivity($Wm^{-1}K^{-1}$)
k^* : Mean absorption coefficient(m^{-1})
Kr : Reaction rate factor(-)
M : Magnetic parameter(-)
Nu : Nusselt number(-)
Le : Lewis number(-)
Nt : Thermophoresis coefficient(-)
Nb : Brownian coefficient(-)
Pr : Prandtl number(-)
R : Radiation factor(-)
S_h : Sherwood number(-)
u : Velocity components along x - axis(ms^{-1})
v : Velocity components along y - axis(ms^{-1})
We : Williamson parameter(-)
x : Coordinate along stretching sheet(m)

Greek Symbols

γ : Angle of inclination(∘)
r : Temporal factor(-)
μ : Fluidity(Pa^{-1} s^{-1})
α : Thermal diffusivity(ms^{-2})
β : Coefficient of casson(-)
β^* : Thermal conductivity coefficient(K^{-1})
β_c : Expansion concentration coefficient(m^3 kg^{-1})
θ : Dimensionless temperature(-)
Φ : Dimensionless concentration(-)
ψ : Fluid motion variable(m^2s^{-1})
σ : Electrical conductivity (Sm^{-1})
σ^* : Stefan Boltzmann constant($Wm^{-1}K^{-4}$)
υ : Viscosity of kinematics(m^2s^{-1})
τ : Heat capacity ratio(-)

Subscripts

w : Surface conditions
∞ : Free stream condition

1. Introduction

MFD is a fascinating science branch that studies the complexities of electrically conducting fluids, such as molten state metals, electrolytes, and saline solutions. The basic goal of MFD flow is to investigate how these fluids behave in the

 Received on: Oct., 2025

presence of magnetic fields. Non-Newtonian fluids have several chemical, pharmaceutical, and cosmetic uses Hopfinger et al. (2008). These fluids are always interesting to researchers because of their scientific and technological uses. The literature has proposed several models for non-Newtonian fluids. The stretching plane irreversibility of MFD was examined by Elnaqeeb et al. (2021). After outlining the characteristics of flow MFD approaching a stretched surface, Pavlov (1974) first gave a precise solution to the momentum equation. MFD's potential to transform industries. Such as energy production and environmental management, is still a fascinating subject for study, with plenty of room for innovations and progress as scientists work to solve its riddles.

Humane et al. (2021) explored non-Newtonian fluids, and there is limited research examining the effects on the behavior of CWFs over-stretching surfaces of magnetic fields, reaction with chemicals, and thermal radiation. Sparrow and Abraham(2005) examined planar edge of layer flow on a non-compressible Newtonian fluid induced by a sheet of elasticity, elongating flat. The velocity of the sheet within the plane increases, and the spacing from the stationary position also increases due to being driven by a uniformly applied stress. Sulochana et al. (2016) investigated 3D-MFD fluid of Newtonian, non-Newtonian motion with mass and transfer of heat on extending surface by the effects of Brownian motion and thermophoresis coefficient.

Abbas et al. (2023) studied CWF on an elongated, non-penetrable sheet in which the localized electrical factor helps enhance field temperature and velocity. At the same time, Casson and porous variables decrease the velocity profiles. Furthermore, Pal et al. (2020) examined fluid flow beneath flexible sheets of varying thickness. The transmission of thermal energy and matter in the boundary layer flow across a stretched sheet was studied by Magyari and Keller et al. (1999). Rana et al. (2017) anticipated boundary effects of inertia by including the velocity square term with the Darcian velocity equation. Hayat et al. (2017) explored Darcy-Forchheimer third-grade material flow, which is enclosed by a linear, elongated, Cattaneo-Christov surface dual diffusion equation to analyze how temperature and concentration are increased via the porosity variable.

Kumar et al. (2017) analyzed the heat transfer characteristics and the flow of the boundary layer of a Williamson fluid containing suspended particles on a widening surface, accounting for the effects of temperature and mass concentration with respect to irregular thermal radiation and the Williamson parameters. Srinivasacharya et al. (2019) determined the Joule heating effect on viscous flow. The elongated surface with convective boundary conditions, such as velocity, temperature, and transfer rates, was analyzed using numerical methods, revealing the magnetic field and Joule heating effects. Ananthaswamy et al. (2019) examined the chemical reaction on mass transfer with respect to the stretched surface. Some researchers, including Takhar et al. (2000)Sangamesh et al. (2025)Vinod et al. (2025) and Vinod and Raghunatha(2024), studied the mass flow on a stretched magnetic field of reacting substances with the n^{th} order. They found that the transfer of mass within the boundary layer, due to an elongated plane within a porous medium, is crucial in the production sector.

Specific research focuses on various MFD applications in environmental management, including energy and industrial processes. We analyzed the effect of multiple criteria on heat, mass and fluid flow properties. It highlights MFD's potential to enhance scientific knowledge and drive industrial advancements in fluid dynamics.

2. Problem Formulation

Under the Williamson and Casson frameworks, based on Cauchy, the tensor stress governed by stress due to shear relationships are presented below.

By the Williamson model

$$\tau_{ij} = \mu \frac{\partial u}{\partial y}\left(1 + \frac{\Gamma}{2}\frac{\partial u}{\partial y}\right) \tag{1}$$

By the Casson model

$$\tau_{ij} = \mu \frac{\partial u}{\partial y}\left(1 + \frac{1}{\beta}\right) \tag{2}$$

In these relations, r, μ and β signify fluid characteristics like the temporal factor, fluidity, and coefficient of Casson, respectively. If time constant is null, the Newtonian formulation of the model is possible, indicates Newtonian model serves as central element of shear stress in absence of time variable. A critical observation is identified as the threshold stress, as the material exhibits zero shear rates due to the effect of infinite viscosity. However, applying shear stress beyond this minimum initiates fluid motion, which is similar to the behavior observed in the Casson model. Finally, the response of fluids incorporates the characteristics of the Williamson-Casson models. Hence, the Casson-Williamson model equation becomes

$$\tau_{ij} = \underbrace{\mu\frac{\partial u}{\partial y}\left(\left(1+\frac{1}{\beta}\right)+\frac{\Gamma}{2}\frac{\partial u}{\partial y}\right)}_{\text{Casson-Williamson Model}} \tag{3}$$

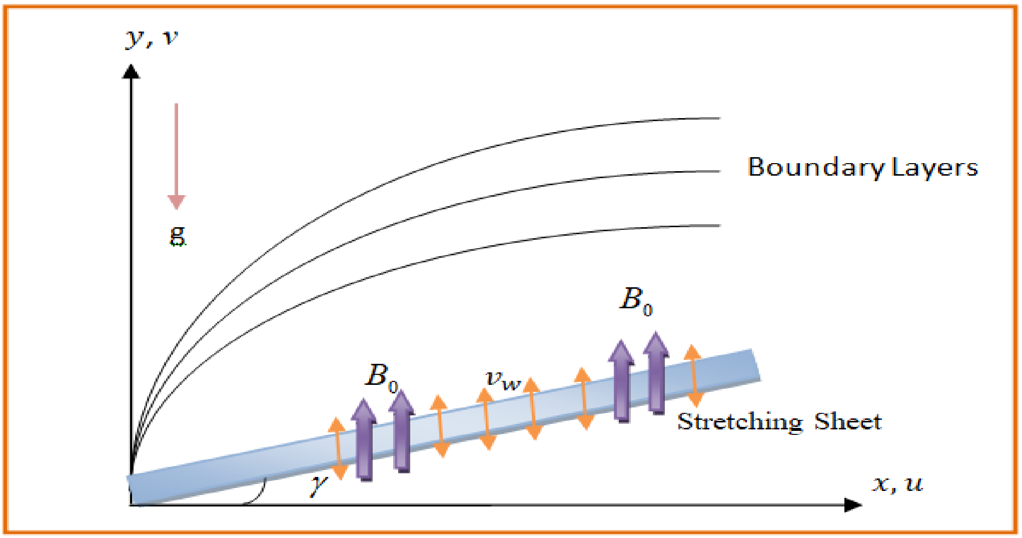

Fig. 1: Flow diagram

This study aims to analyze the impacts of magnetic fields, chemical reactions, and thermal barriers on heat transfer characteristics in MFD-CWF. The CWF studies incorporate the flow of fluid dynamics over an elongated layer. The beginning of the process is the expansion of a uniformly penetrable substance in a fixed position near the aperture. On the contrary, the fixed position may be stationary on a plane or merged into a porous medium, indicated in Fig. 1. In this study, the complete flow of fluid affected by the effects of heat and the uniform ascending field around the magnet effects the strength, which is indicated by B_0, opposing the surface. The vertical surface is along the y-axis, and x-axis is normal to y-axis. Where u and v are velocity components along x-axis and y-axis. This model assumes steady and laminar conditions, which is considered adequate and may be due to non-Newtonian fluids over an extensive array of stress rates. Further, the induced magnetic Reynolds number flow is minimal, neglecting caused magnetic field. It indicates no suction at fixed boundaries. Here, T, C and ρ represents the temperature of the fluid, concentration, and the fluid density, respectively. This Casson-Williamson model for two-dimensional, incompressible flow is regulated by a mathematical model system with derivatives tailored to this scenario. The study investigates phenomena such as the convection heat transfer method and the absorption effect on an extended plate. It explains an innovative approach, extending existing models and incorporating critical parameters into studying elements. Mathematical concepts for the flow are formulated based on frameworks developed by Khan et al. (2023) and Humane et al. (2021). Furthermore, refinement and enhancements of the above probable concepts can be used.

The governing equations are as follows(Khan et al., 2024):

$$\frac{\partial u}{\partial x}+\frac{\partial v}{\partial y}=0 \tag{4}$$

$$u\frac{\partial u}{\partial x}+v\frac{\partial u}{\partial y}=\upsilon\left(1+\frac{1}{\beta}\right)\frac{\partial^2 u}{\partial y^2}+\sqrt{2}\upsilon\Gamma\frac{\partial u}{\partial y}\frac{\partial^2 u}{\partial y^2}-\frac{\sigma B_0^2 u}{\rho}-\frac{C_b u^2}{\sqrt{k}}+\left[g\beta_c\left(C-C_\infty\right)+g\beta^*\left(T-T_\infty\right)\right]\cos\gamma \tag{5}$$

$$u\frac{\partial T}{\partial x}+v\frac{\partial T}{\partial y}=\alpha\left(1+\frac{16T_\infty^3\sigma^*}{3kk^*}\right)\frac{\partial^2 T}{\partial y^2}+\tau\left[\left(\frac{\partial T}{\partial y}\right)^2\frac{D_T}{T_\infty}+D_B\frac{\partial C}{\partial y}\frac{\partial T}{\partial y}\right]+\frac{\mu}{\rho C_p}\left(\frac{\partial u}{\partial y}\right)^2+\frac{\sqrt{2}\Gamma\mu}{\rho C_p}\left(\frac{\partial u}{\partial y}\right)^3+\frac{\sigma B_0^2 u^2}{\rho C_p} \tag{6}$$

$$u\frac{\partial C}{\partial x}+v\frac{\partial C}{\partial y}=D_B\frac{\partial^2 C}{\partial y^2}+\frac{D_T}{T_\infty}\frac{\partial^2 T}{\partial y^2}-K_r\left(C-C_\infty\right) \tag{7}$$

Velocity induced by gravitational force is expressed by$g$, where β^*, and β_c represents the thermal conductivity coefficient and expansion concentration coefficients. Thermal conductivity is represented as k, and mean of absorption coefficient as k^*, Stefan Boltzmann constant is typically described as σ^*. The system mentioned has numerous variables, such as ν and αrepresenting the viscosity of kinematics and thermal diffusivity, respectively. The heat capacity ratio of particles compared to a regular fluid is measured by τ, heat capacity at constant pressure is denoted by C_p, the angle of inclination by γ, coefficient of Brownian diffusion by D_B, coefficient of thermophoretic diffusion symbolized as D_T, the electrical conductivity is denoted as σ, and K_r reflects the reaction rate factor. Ambient parameters representing temperature, velocity, and solute concentration are expressed as T_∞, U_∞, and C_∞, respectively. Below are relevant boundary conditions (Khan et al., 2023).

$$\left.\begin{array}{l}\text{at, } y=0:\ u=U_w=bx,\ v=-v_w,\ T=T_w,\ C=C_w \\ \text{as, } y\to\infty:\ u=0,\ T=T_\infty,\ C=C_\infty\end{array}\right\} \tag{8}$$

Where U_w, T_w and C_w represents velocity, temperature and concentration at the surface, respectively.
Similarity conversions to address mathematical modeling equations (4)-(8) are used as

$$\eta = y\sqrt{\frac{b}{\nu}},\ v=-\sqrt{b\nu}\, f(\eta),\ u=bxf'(\eta),\ \theta(\eta)=\frac{T-T_\infty}{T_w-T_\infty} \text{ and } \phi(\eta)=\frac{C-C_\infty}{C_w-C_\infty}.$$

This approach introduced the equivalent transformation by applying η as a similarity variable. *f(η)* Represents a fluid motion variable, *θ(η)* is the dimensionless representation of temperature, and *Φ(η)* is the dimensionless concentration function. The flow patterns are defined by *ψ(x, y)*, presented as $u=\frac{\partial\psi}{\partial y}$, $v=-\frac{\partial\psi}{\partial x}$, which satisfies Equation (1) by testing the second-order η-derivative and then applying it to relations (5) – (7).
The PDEs are converted into a group of ODEs (9)–(11)

$$\left(1+\frac{1}{\beta}\right)f'''+We\, f'''\, f''-f'^2+ff''-Mf'-Fr\, f'^2+\left[Gc\ \phi(\eta)+Gr\ \theta(\eta)\right]\cos\gamma=0 \tag{9}$$

$$\frac{1}{\Pr}\left(1+\frac{4R}{3}\right)\theta''+Nb\ \theta'\phi'+f\theta'+Nt\ \theta'^2+Ec\ \left[We\, f''^3+Mf'^2+f''^2\right]=0 \tag{10}$$

$$\phi''+\left(\frac{Nt}{Nb}\right)\theta''+Le\, f\phi'-LeG\phi=0 \tag{11}$$

In the above equations, the factors *G, Le, We, Ec, Nt, Nb, R, Pr, Gc, Gr, Fr, M, β* and *γ* represent the chemical reaction coefficient, Lewis number, Williamson parameter, Eckert number, thermophoresis coefficient, Brownian coefficient, radiation factor, Prandtl number, Solutal factor, Grashof number, Forchheimer number, magnetic parameter, Casson parameter, and angle of inclination, respectively.

The corresponding boundary conditions are

$$\left.\begin{array}{l}f(\eta)=f_w,\ \ f'(\eta)=\lambda,\ \ \theta(\eta)=1,\ \ \phi(\eta)=1 \text{ at } \eta=0 \\ f'(\eta)=\theta(\eta)=\phi(\eta)=0 \text{ at } \eta=\infty\end{array}\right\} \tag{12}$$

The parameters included in the equations (9)-(12) are listed below:

$$We=x\Gamma\sqrt{\frac{2b^3}{\nu}},\ Fr=\frac{C_b x}{\sqrt{k}},\ Le=\frac{\nu}{D_B},\ \Pr=\frac{\nu}{\alpha},\ Ec=\frac{U_w^2}{\left(T_w-T_\infty\right)C_p}, Nt=\frac{\tau D_T\left(T_w-T_\infty\right)}{\nu T_\infty},\ Nb=\frac{\tau D_B\left(C_w-C_\infty\right)}{\nu}$$

$$M=\frac{\sigma B_0^2}{b\rho},\ Gr=\frac{g\beta^*(T_w-T_\infty)}{b^2x},\ Gc=\frac{g\beta_c\left(C_w-C_\infty\right)}{b^2x},\ G=\frac{K_r}{b},\ \ R=\frac{4\sigma^* T_\infty^3}{kk^*}.$$

3. Numerical Outcome

To compute the stated problem, higher-order ODEs were modified to first-order ODEs. Then, we applied the Matlab-based BVP4C algorithm, which is an integral part of the finite difference method. This approach is based on primary assumptions to address boundary value problems. For more information on BVP4C, you can refer to Keskin. This MATLAB algorithm helps solve higher-order differential equations by making it a flexible option for science, technical, mathematics, and engineering. To obtain the outcome by the BVP4C Matlab built-in function, defined new variables which are

$$\left.\begin{array}{l}f(\eta)=y_1,\ f'(\eta)=y_2,\ f''(\eta)=y_3,\ \theta(\eta)=y_4,\ \theta'(\eta)=y_5, \\ \phi(\eta)=y_6,\ \phi'(\eta)=y_7,\ \theta''(\eta)=yy_2,\ \ f'''(\eta)=yy_1,\ \phi''(\eta)=yy_3\end{array}\right\} \tag{13}$$

After incorporating these variables, we obtained the following equations:

$$\left. yy_1=\frac{M\ y_2+Fr\ y_2^2+y_2^2-y_1\ y_3-\left(Gc\ y_6+Gr\ y_4\right)\cos\gamma}{\left(1+\frac{1}{\beta}\right)+We\ y_3}\right\} \tag{14}$$

$$yy_2 = -\Pr \frac{\left(Nb\, y_5 y_7 + y_1 y_5 + Nt\, y_5^2 + Ec\left(We\, y_3^3 + y_2^2 M + y_3^2\right)\right)}{\left(1+\dfrac{4R}{3}\right)} \tag{15}$$

$$yy_3 = -\frac{Nt}{Nb} yy_2 - Le\, y_1 y_7 + Le\, G y_6 \tag{16}$$

In addition to the given constraints, the boundary conditions are

at $\eta = 0,\ y_1 = f_w,\ y_2 = \lambda,\ y_4 = 1,\ y_6 = 1,$

as $\eta \to \infty,\ y_2 = 0,\ y_4 = 0,\ y_6 = 0.$ (17)

We used these equations (14)-(16) in the BVP4C Matlab built-in function by applying boundary conditions (17). Also, for engineering purposes, the skin friction coefficient(C_f), Nusselt number(N_u), and Sherwood number(S_h) Karthikeyan et al. (2016)are as described

$$\mathrm{Re}_x^{1/2} C_f = f''(0),\ \mathrm{Re}_x^{-1/2} Nu = -\left(1+\frac{4R}{3}\right)\theta'(0) \text{ and } \mathrm{Re}_x^{-1/2} Sh = -\phi'(0). \tag{18}$$

4. Outcomes and Interpretation

In this investigation, we examined phase diagrams in-depth to explore how different dimensionless parameters impact fluid speed, thermal transfer, and mass distribution. Advanced mathematical modeling in MATLAB was employed to generate a graphical representation, highlighting the unique characteristics of the problem. This investigation addressed Williamson and Casson's fluid flows with multiple physical factors. A flowchart was developed to illustrate mass transport under varying conditions, accompanied by detailed insights into temperature and velocity profiles. The analysis included extensive numerical computations using the subsequent constant parameters, *Fr=0.3, Gc=0.2, Nt=0.1, Pr=0.3, Gr=0.2, G=0.7, Le=0.3, R=0.2, M=2, Ec=0.4, Nb=0.2, γ=π/6, Fw=0.5* and *λ=1.*

These variables stayed the same throughout the study unless varying values were mentioned in the specific graphs and tables. This arrangement strongly supports our analysis. Fig. 2 depicts how the magnetic field parameter influences fluid velocity. *M* as the fluid velocity takes a higher value, fluid velocity decreases, reducing the boundary layer. The decrease in velocity of the fluid is due to the resistive force. Fig. 3 indicates an enhancement in thermal properties under the influence of *M*. This improvement in magnetic field strength is due to the application of normal energy to the conducting fluid. An electrostatic field interacts with an insulating liquid, generating a force termed the Lorentz force. Although this force opposes the motion of the fluid, it reduces the flow rate inside the boundary layer. Lorentz force impacts the drag coefficient, introducing a supply of energy and augmenting thermal efficiency in the flow system.

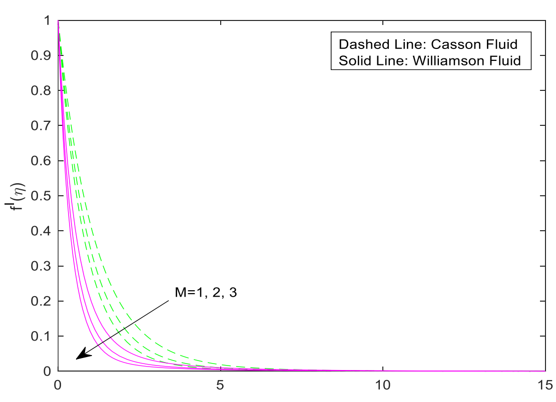

Fig. 2: Exhibits *f'(η)* changes via *M*

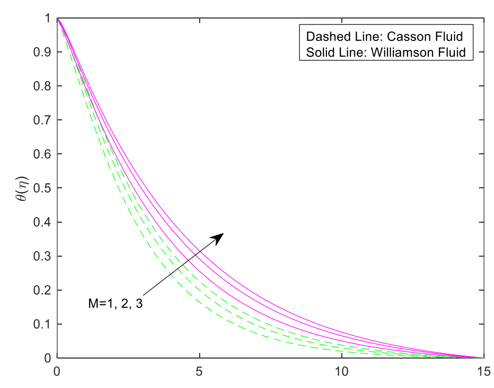

Fig. 3: Exhibits *θ(η)* changes via *M*

The velocity variation shown in Fig. 4 illustrates how the Prandtl number impacts various fluid properties. As *Pr* increases the temperature of liquid decreases. This is because a higher *Pr* value means the thermal conductivity of the fluid is lower. When thermal conductivity reduces, heat does not transfer as effectively, leading to a drop in temperature. In contrast, the concentration profile behaves differently. As *Pr* enhances, thermal boundary layer thickness becomes smaller. It indicates that the influence of the Prandtl number affects how heat is distributed and retained within the fluid. Consequently, it leads to a decrease in *θ(η)* profile. Fig. 5 indicates the effect of *R* on temperature. The graph explains that the conviction effect increases the increment of the energy profile. In this case, energy accumulated depends on the radiation effect, thereby increasing heat distribution in the fluid boundary layer. The impact of *Ec* on temperature profile is depicted in Fig. 6. The Graph shows that the values of *Ec* rise, the temperature of the wall surface grows, and the thermal boundary layer rises.

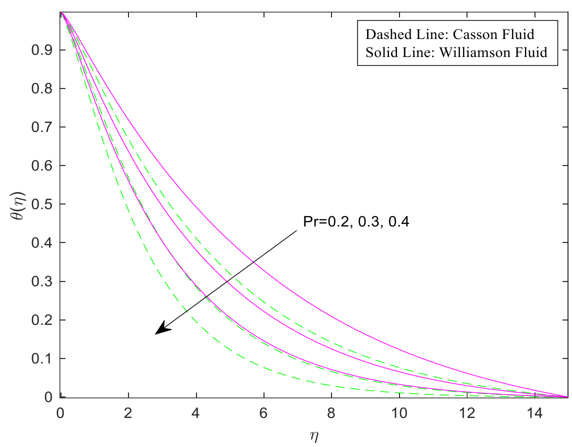

Fig. 4: Exhibits *θ(η)* changes via *Pr*

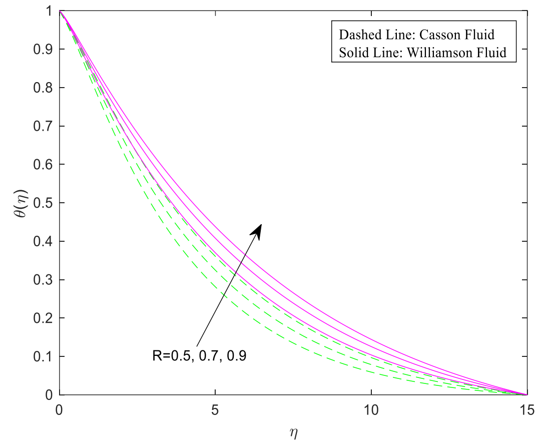

Fig. 5: Exhibits *θ(η)* changes via *R*

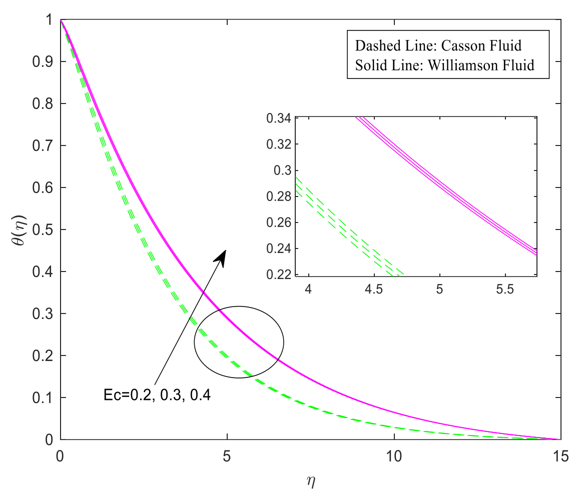

Fig.6: Exhibits *θ(η)* changes via *Ec*

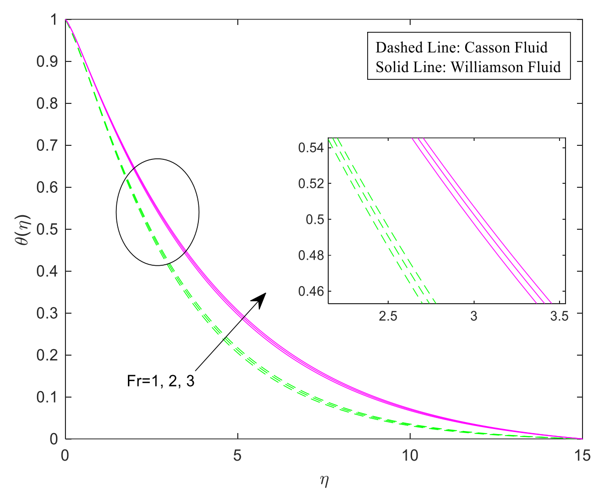

Fig. 7: Exhibits *θ(η)* changes via *Fr*

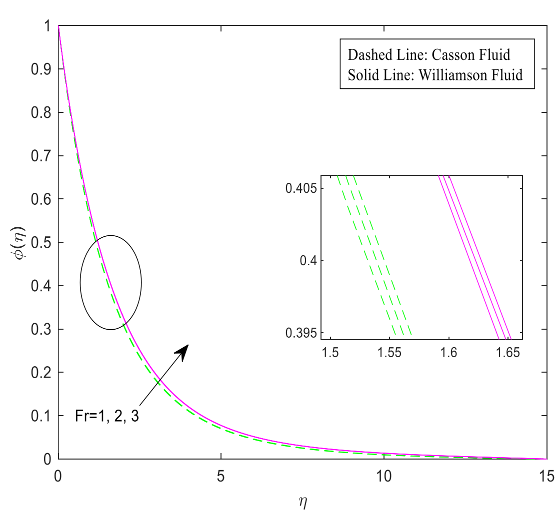

Fig. 8: Exhibits *ϕ(η)* changes via *Fr*

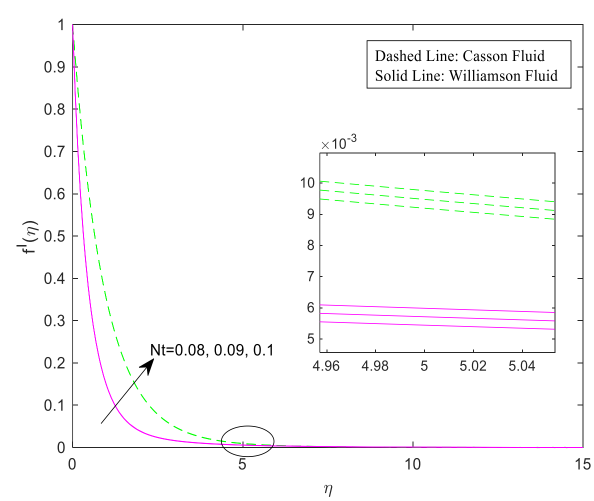

Fig. 9: Exhibits *f'(η)* changes via *Nt*

Figs. 7 and 8 show the plots of *θ(η)* and *Φ(η)* against the Forchheimer number *Fr*. The results demonstrate that *θ(η)* and *Φ(η)* increases as the Forchheimer number enhances. Physically, heat convection is accelerated by greater friction, and the resistive force is caused by inertia. Therefore, the dispersion of temperature and concentration strengthens as *Fr* increases. From Figs. 9 and 10, the velocity and concentration profile also rise as the thermophoresis parameter goes up. Thermophoresis is a characteristic that helps to increase the thickness of fluid flow and concentration boundary layers. Consequently, both profiles are elevated.

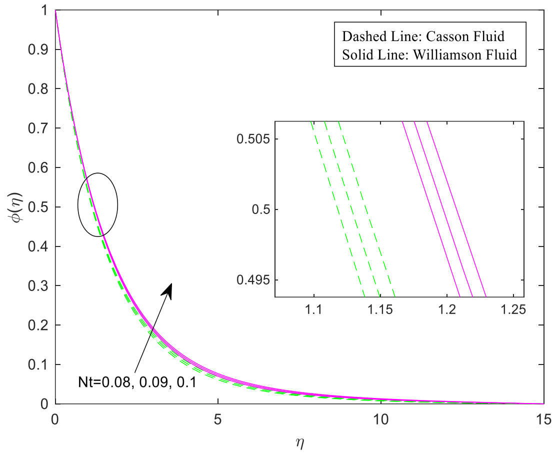

Fig. 10: Exhibits $\phi(\eta)$ changes via *Nt*

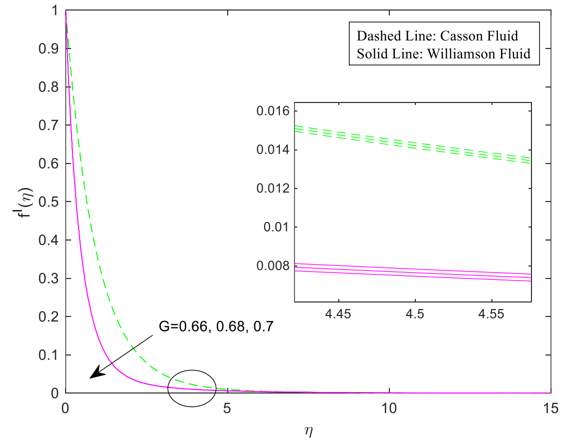

Fig. 11: Exhibits $f'(\eta)$ changes via *G*

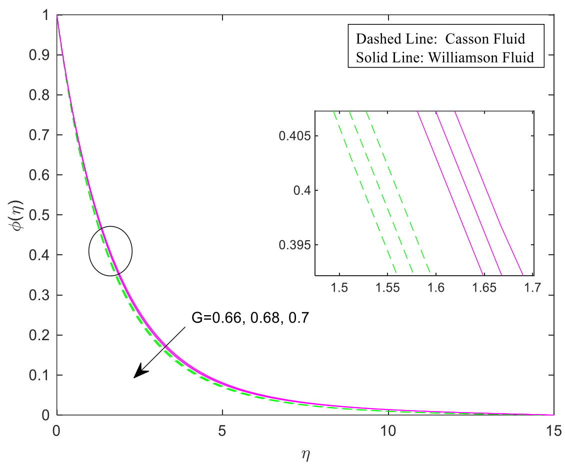

Fig. 12: Exhibits $\phi(\eta)$ changes via *G*

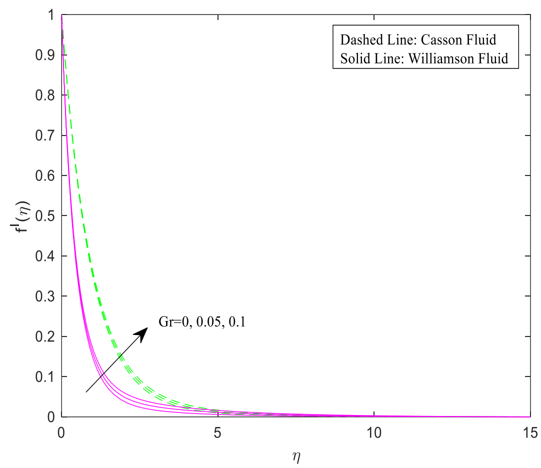

Fig. 13: *Exhibits* $f'(\eta)$ changes via *Gr*

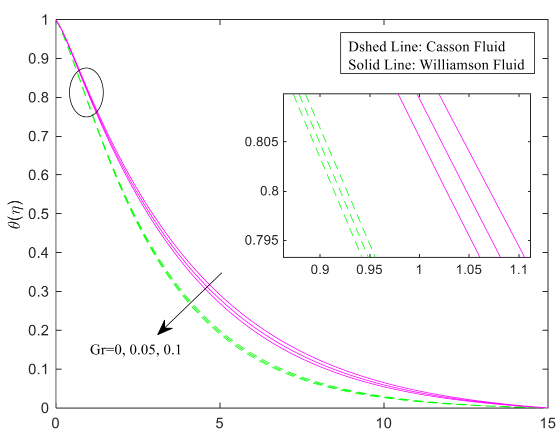

Fig. 14: Exhibits $\theta(\eta)$ changes via *Gr*

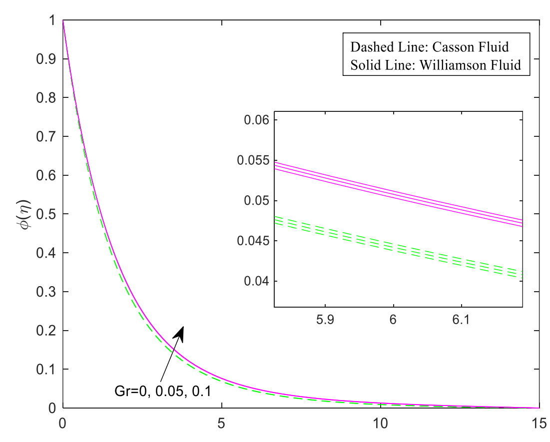

Fig. 15: Exhibits $\phi(\eta)$ changes via *Gr*

As shown in Figs. 11 and 12, the dimensionless $f'(\eta)$ and $\Phi(\eta)$ diminishes as the chemical reaction parameter *G* improves. The reason for this is that faster chemical reactions lower fluid motion and the concentration. The implications of *Gr* on velocity, temperature and concentration distribution are depicted in Figs 13, 14, and 15**,** respectively. As demonstrated, velocity and concentration rise as *Gr* grows, but the temperature shows the reverse tendency. As *Gr* the buoyant forces increase, the concentration buoyancy parameter increases. It is due to larger values of *Gr* corresponding to stronger buoyancy forces. This causes fluid to accelerate, growing fluid velocities and concentration, which subsequently reduces $\theta(\eta)$. The impact of local solutal Grashof number *Gc* on concentration is depicted in Fig 16. As *Gc* improves, the $\Phi(\eta)$ drops, demonstrate the typical phenomenon that *Gc* stabilizes the expansion of the boundary layer.

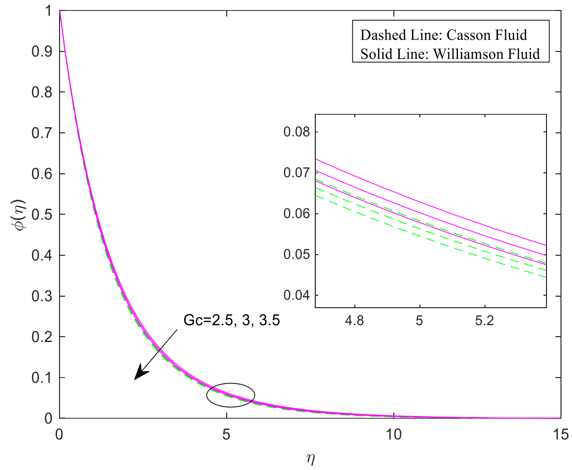

Fig. 16: Exhibits $\phi(\eta)$ changes via *Gc*

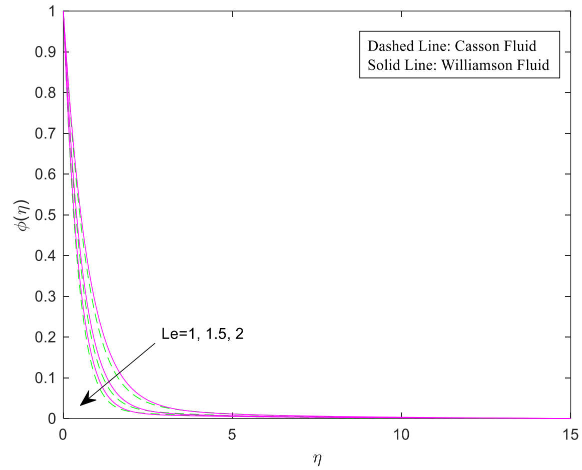

Fig. 17: Exhibits $\phi(\eta)$ changes via *Le*

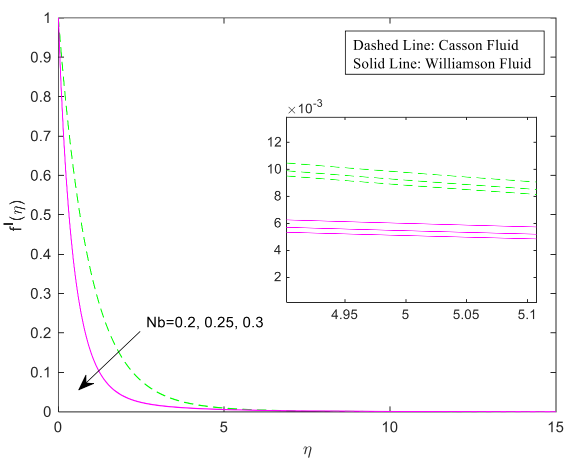

Fig. 18: Exhibits $f'(\eta)$ changes via *Nb*

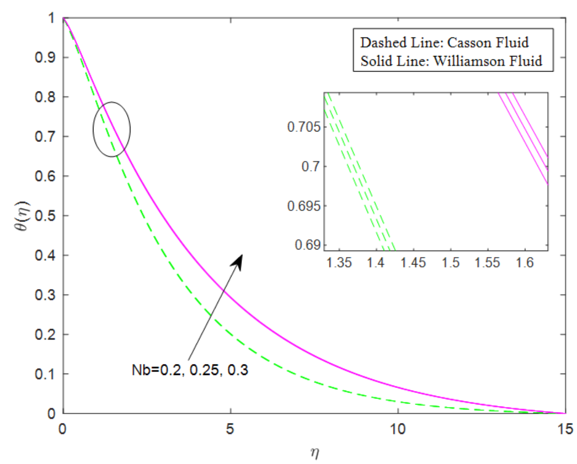

Fig. 19: Exhibits $\theta(\eta)$ changes via *Nb*

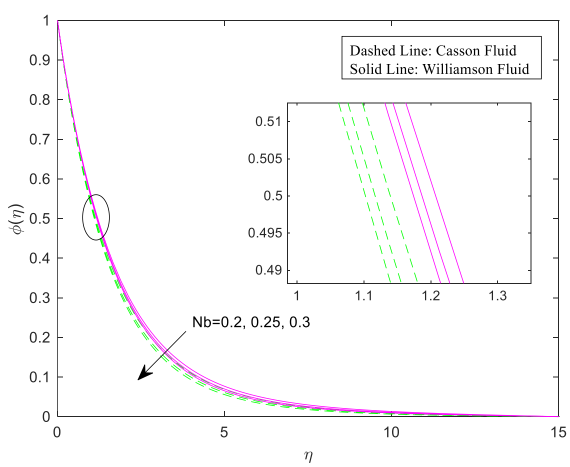

Fig. 18: Exhibits $f'(\eta)$ changes via *Nb*

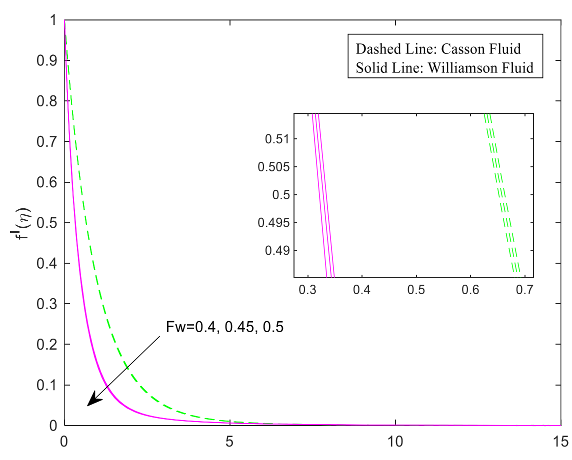

Fig. 19: Exhibits $\theta(\eta)$ changes via *Nb*

Fig. 17 displays effect of variation in Lewis number *Le* on solubility profile. Notably, as *Le* expands, solubility decreases significantly. The stated effect is due to the Lewis number, which causes the solubility boundary layer to become thinner. Figs 18, 19 and 20 depict impact of Brownian motion on velocity, temperature and concentration field. As *Nb* increases, both $f'(\eta)$ and $\Phi(\eta)$ decreases, while $\theta(\eta)$ intensifies rapidly. Figs. 21, 22, and 23 provided the outcome of distributions of $f'(\eta)$, $\theta(\eta)$ and $\Phi(\eta)$ for multiple values of the suction parameter *Fw*. The concentration, temperature, and velocity profiles diminish as the suction parameter increases. It implies that the thinner the boundary layer induced by the suction parameter, the better for fluid flow stability.

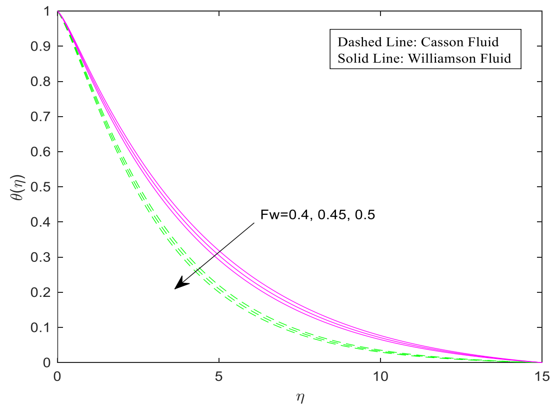

Fig. 22: Exhibits $\theta(\eta)$ changes via *Fw*

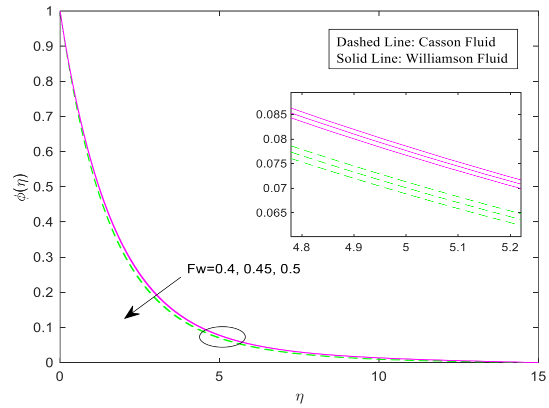

Fig. 23: Exhibits $\phi(\eta)$ changes via *Fw*

Tables 1 and 2 represent values of skin friction coefficient(C_f), Nusselt number(N_u) and Sherwood number(S_h) for Casson and Williamson fluids under various relevant governing parameters. It is observed that the C_f and N_u in both CWF decreases for different values of increasing governing constraints *M, Ec, Fr, G*, and *Nu*. And the C_f and N_u have opposite trends, i.e., growing with rising values of *Pr, Gc* and *Gr*. Further, we noticed that the Sherwood number in both Casson and Williamson fluid increases with enhancing values of *M, Ec, G, Gr, Gc, Fr*, and *Le*, and decreases with increasing values of *Fr*. A comparison of the current result for thermal profile with the results of Yousef et al. (2022)is presented in Table 3. The table shows that the results are in good agreement.

Table 1: The C_f , N_u and S_h for Casson and Williamson fluids under various relevant parameters *M, Pr, Fr*, and *Ec*

M	*Pr*	*Fr*	*Ec*	$\mathrm{Re}_x^{1/2}\, C_f$		$\mathrm{Re}_x^{-1/2}\, Nu$		$\mathrm{Re}_x^{-1/2}\, Sh$	
				Casson Fluid	Williamson Fluid	Casson Fluid	Williamson Fluid	Casson Fluid	Williamson Fluid
1				-2.696489	-1.930518	0.271595	0.198890	0.615698	0.604663
2				-3.240874	-2.419158	0.191813	0.142490	0.632495	0.613454
3				-3.702322	-2.893052	0.129953	0.104121	0.646540	0.619658
	0.2			-3.242951	-2.420453	0.147215	0.113866	0.636620	0.612850
	0.3			-3.240874	-2.419158	0.191813	0.142490	0.632495	0.613454
	0.4			-3.238940	-2.417730	0.233648	0.173459	0.626675	0.611618
		1		-3.456498	-2.625171	0.188398	0.139759	0.631420	0.612518
		2		-3.743266	-2.418522	0.183658	0.136509	0.630207	0.611232
		3		-4.009661	-3.235964	0.179092	0.134007	0.629280	0.609937
			0.2	-3.239963	-2.418522	0.274883	0.213592	0.603106	0.587158
			0.3	-3.240418	-2.418844	0.233347	0.178042	0.617800	0.600306
			0.4	-3.240874	-2.419158	0.191813	0.142490	0.632495	0.613454

Table 2: The C_f , N_u and S_h for Casson and Williamson fluids under various relevant parameters *Gr, Gc, Le*, and λ

Gr	*Gc*	*Le*	λ	$\mathrm{Re}_x^{1/2}\, C_f$		$\mathrm{Re}_x^{-1/2}\, N_u$		$\mathrm{Re}_x^{-1/2}\, S_h$	
				Casson Fluid	Williamson Fluid	Casson Fluid	Williamson Fluid	Casson Fluid	Williamso n Fluid
0				-3.240874	-2.419158	0.191813	0.142490	0.632495	0.613454
0.05				-3.203596	-2.374992	0.194565	0.149146	0.632823	0.613704
0.1				-3.166602	-2.331961	0.197116	0.155193	0.633180	0.614019
	2.5			-1.996844	-1.135738	0.224485	0.223399	0.649315	0.634888
	3			-1.740398	-0.916738	0.225019	0.227346	0.654033	0.641299

	3.5			-1.488317	-0.711065	0.224038	0.228332	0.658973	0.648106
		1.0		-3.282097	-2.459263	0.186004	0.131922	1.363692	1.313580
		1.5		-3.294482	-2.473756	0.185172	0.129922	1.782444	1.721599
		2.0		-3.302514	-2.483894	0.184837	0.128944	2.164838	2.097157
			0.8	-2.472216	-1.725254	0.218956	0.172999	0.603293	0.590612
			0.9	-2.851227	-2.052006	0.207099	0.158519	0.617386	0.601895
			1.0	-3.240874	-2.419158	0.191813	0.142490	0.632495	0.613454

Table 3: Comparison of $Re_x^{-1/2}Nu$ with the results of Yousef et al. (2022) for the limiting case when $M=We=Nb=0.5$, $G=0.2$, $Fr=0.5$, $Gc=Fw=\gamma=0$, $Nt=0.1$, $\lambda=1$, $Pr=2.0$, $Gr=0.2$, $Le=0.7$ and $R=0.2$

Ec	Yousef et al. [25]	Present outcome
0.1	0.372781	0.372782
0.2	0.342993	0.342994
0.3	0.198511	0.198511

5. Conclusions

In this investigation, we examined the numerical solution for fluid flow, focusing on the effects of a magnetic force on a stretched surface inclined at an angle γ. We utilized Matlab's BVP4C tools to solve fundamental governing non-dimensional equations. Results were shown using visual graphs and tabulated data, clearly showing the main elements of the framework and its physical dynamics. We evaluated the outcome against established data derived under various assumptions through comprehensive numerical and graphical evaluations to assess the results thoroughly. The detailed analysis shows a strong correlation between our results and previous studies.

The main findings from our study are summarized below:

1. Increasing the value of *M* results in reduced fluid velocity due to the Lorentz force and enhanced energy generation in the flow.
2. A higher Prandtl number(*Pr*) indicates a reduced fluid temperature, simultaneously decreasing the thermal boundary layer.
3. A higher Grashof number strengthens the buoyancy force, causing a growth in fluid velocity.
4. The thermophoresis coefficient enhances particle solubility near heated surfaces, increases the thermal boundary layer, and impacts thermal diffusivity and mass diffusion.

Our results reveal intricate connections among fluid characteristics that impact velocity, temperature, and concentration distributions. These findings are valuable across diverssified disciplines, ranging from engineering to environmental science, offering opportunities for optimizing processes and systems. The above-stated studies establish a solid groundwork for futureexploration in this area.

Scope for Further Studies:

This study establishes a strong foundation for further studies on fluid flow dynamics and its applications in engineering. Our research enhances the comprehension of sustained behavior in the MFD CWF arrangement, providing an essential understanding of the effects on different fluid dynamics and heat transfer factors. It can be extended to three dimensional flow with respect to CWF and the study of oule heating effect, blood flow w.r.t magnetic effect and entropy related studies.

References

Abbas, W., Megahed, A.M., Ibrahim, M.A. and Said, A.A., 2023. Ohmic dissipation impact on flow of Casson-Williamson fluid over a slippery surface through a porous medium: W Abbas et al. Indian Journal of Physics, 97(14), pp.4277-4283. https://doi.org/10.1007/s12648-023-02754-4

Ananthaswamy, V., Seethalakshmi, B. and Santhi, V.K., 2019. Mathematical analysis on the effect of chemical reaction on mass transfer over a stretching surface embedded in a porous medium. Advances in Mathematics: Scientific Journal, 8(3), pp.266–275. https://www.researchgate.net/publication/340575026

Elnaqeeb, T., Animasaun, I.L. and Shah, N.A., 2021. Ternary-hybrid nanofluids: significance of suction and dual-stretching on three-dimensional flow of water conveying nanoparticles with various shapes and densities. Zeitschrift für Naturforschung A, 76(3), pp.231-243. https://doi.org/10.1515/zna-2020-0317

Hayat, T., Haider, F., Muhammad, T. and Alsaedi, A., 2017. An optimal study for Darcy-Forchheimer flow with generalized Fourier's and Fick's laws. Results in physics, 7, pp.2878-2885. https://doi.org/10.1016/j.rinp.2017.08.002

Hopfinger, E.J., Aliseda, A., Kremer, D.M., Berchielli, A., Connelly, E.K. and Lasheras, J.C., 2007. Atomization of Non-Newtonean liquids by a high momentum coaxial gas jet. APSBulletin, Vol. 52, No. 17. https://doi.org/10.1016/j.ijmultiphaseflow.2007.09.003

Humane, P.P., Patil, V.S. and Patil, A.B., 2021. Chemical reaction and thermal radiation effects on magnetohydrodynamics flow of Casson–Williamson nanofluid over a porous stretching surface. Proceedings of the Institution of Mechanical Engineers, Part E: Journal of Process Mechanical Engineering, 235(6), pp.2008-2018. https://doi.org/10.1177/09544089211025376

Karthikeyan, S., Bhuvaneswari, M., Sivasankaran, S. and Rajan, S., 2016. Soret and Dufour effects on MHD mixed convection heat and mass transfer of a stagnation point flow towards a vertical plate in a porous medium with chemical reaction, radiation and heat generation. https://doi.org/10.18869/acadpub.jafm.68.228.24135

Khan, K.A., Javed, M.F., Ullah, M.A. and Riaz, M.B., 2023. Heat and Mass transport analysis for Williamson MHD nanofluid flow over a stretched sheet. Results in Physics, 53, p.106873. https://doi.org/10.1016/j.rinp.2023.106873

Khan, K.A., Vivas-Cortez, M., Ahammad, N.A., Bushra, H., Gamaoun, F., Javed, M.F. and Raza, N., 2024. Unfolding some numerical solutions for the magnetohydrodynamics Casson–Williamson nanofluid flow over a stretching surface. Journal of Computational Design and Engineering, 11(3), pp.1-11. https://doi.org/10.1093/jcde/qwae036

Kumar, K.G., Rudraswamy, N.G., Gireesha, B.J. and Manjunatha, S., 2017. Non linear thermal radiation effect on Williamson fluid with particle-liquid suspension past a stretching surface. Results in Physics, 7, pp.3196-3202.https://doi.org/10.1016/j.rinp.2017.08.027

Magyari, E. and Keller, B., 1999. Heat and mass transfer in the boundary layers on an exponentially stretching continuous surface. Journal of Physics D: Applied Physics, 32(5), pp.577-585. https://doi.org/10.1088/0022-3727/32/5/012

Pal, D., Chatterjee, D. and Vajravelu, K., 2020. Influence of magneto-thermo radiation on heat transfer of a thin nanofluid film with non-uniform heat source/sink. Propulsion and Power Research, 9(2), pp.169-180. https://doi.org/10.1016/j.jppr.2020.03.003

Pavlov, K.B., 1974. Magnetohydrodynamic flow of an incompressible viscous fluid caused by deformation of a plane surface. Magnitnaya Gidrodinamika, 4(1), pp.146-147.

Rana, B.J., Roy, R., Ali, L.E. and Ahmmed, S.F., 2017. Radiation absorption and variable electrical conductivity effect on high speed MHD free convective flow past an exponential accelerated inclined plate. World Journal of Mechanics, 7(08), pp.211-241. https://doi.org/10.4236/wjm.2017.78019

Sangamesh, Raghunatha, K.R. and Vinod, Y., 2025. Analysis of MHD two-phase nanofluid with dufour and soret effects over an exponentially permeable surface. International Journal of Applied and Computational Mathematics, 11(2), p.25. https://doi.org/10.1007/s40819-025-01835-8

Sparrow, E.M. and Abraham, J.P., 2005. Universal solutions for the streamwise variation of the temperature of a moving sheet in the presence of a moving fluid. International Journal of Heat and Mass Transfer, 48(15), pp.3047-3056. https://doi.org/10.1016/j.ijheatmasstransfer.2005.02.028

Srinivasacharya, D. and Jagadeeshwar, P., 2019. Effect of Joule heating on the flow over an exponentially stretching sheet with convective thermal condition. Mathematical Sciences, 13(3), pp.201-211. https://doi.org/10.1007/s40096-019-0290-8

Sulochana, C., Ashwinkumar, G.P. and Sandeep, N., 2016. Similarity solution of 3D Casson nanofluid flow over a stretching sheet with convective boundary conditions. Journal of the Nigerian Mathematical Society, 35(1), pp.128-141. https://doi.org/10.1016/j.jnnms.2016.01.001

Takhar, H.S., Chamkha, A.J. and Nath, G., 2000. Flow and mass transfer on a stretching sheet with a magnetic field and chemically reactive species. International Journal of Engineering Science, 38(12), pp.1303-1314. https://doi.org/10.1016/S0020-7225(99)00079-8

Vinod, Y. and Raghunatha, K.R., 2024. Two numerical methods for thermohaline convection in MHD squeezing flow of Casson fluid saturated porous layer. International Journal of Applied and Computational Mathematics, 10(6), p.161. https://doi.org/10.1007/s40819-024-01795-5

Vinod, Y., Raghunatha, K.R., Nagappanavar, S.N., Nazarova, N. and Gupta, M., 2025. Boundary layer flow of a non-Newtonian fluid over an exponentially stretching sheet with the presence of a heat source/sink. Partial Differential Equations in Applied Mathematics, 13, p.101111. https://doi.org/10.1016/j.padiff.2025.101111

Yousef, N.S., Megahed, A.M., Ghoneim, N.I., Elsafi, M. and Fares, E., 2022. Chemical reaction impact on MHD dissipative Casson-Williamson nanofluid flow over a slippery stretching sheet through porous medium. Alexandria Engineering Journal, 61(12), pp.10161-10170.